

**Title:**

**Investigating the Interaction between SARS-CoV-2 NSP15 and RNF41 Using In Silico Methods**

**Condensed Title:**

**Docking of SARS-CoV-2 NSP15 and RNF41**

**Authors**

**<sup>1</sup>Annika Viswesh,**

**<sup>1,2</sup>Soichi Wakatsuki**

**Affiliations:**

**<sup>1</sup>Structural Biology Department, Stanford University, Stanford, CA 94305**

**<sup>2</sup>SLAC National Accelerator Laboratory**

## **Abstract**

Patients with acute respiratory distress due to SARS-CoV-2 infection exhibit hyper-inflammatory response and Type 1 Interferon (IFN-1) deficiency. Research has shown that RNF41, a human E3 ubiquitin ligase, controls inflammation and IFN-1 production by binding to USP8, MYD88 and TBK1 in the immune signaling pathways. Studies indicate that SARS-CoV-2 NSP15 in addition to cleaving the viral RNA to evade the human immune system also suppresses the immune response; however, the suppression mechanism hasn't been investigated at a molecular level. We hypothesized that SARS-CoV-2 NSP15 can bind to RNF41 and inhibit RNF41 from regulating the immune signaling pathways. Molecular docking of RNF41 C-terminal domain (CTD) to MYD88, TBK1, USP8, and five NSP15 surfaces were performed. Previously unknown structure of RNF41 Zinc-finger domain (ZFD) was generated using homology modeling. Interaction surfaces sites on RNF41 ZFD were determined by developing computational techniques to explore ~170,000 structures in the PDB to filter structures having a structural alignment score of < 2 Å with RNF41 ZFD, and subsequently docked to NSP15. Results show that NSP15, TBK1, MYD88, and USP8 bind to the same residues of RNF41 CTD. NSP15 has the highest binding affinity to RNF41 CTD. Molecular Dynamics (MD) simulations on the binding of RNF41 CTD with NSP15 reaches equilibrium at 7 ns with 83% of the binding residues having lower than average fluctuations which indicate that the binding is stable. This confirmed our hypothesis that NSP15 can bind to RNF41 CTD which can disrupt the immune system's response. Further, NSP15's interaction surfaces encompassing two protomers were located at least 10 Å away from its catalytic site, indicating NSP15's cleaving function could continue even when NSP15 binds to RNF41 CTD. These results advance our understanding of how NSP15 interferes with the immune signaling pathways and will aid in the development of new antiviral therapeutics.

## **Statement of Significance**

The Coronavirus disease 2019 (COVID-19) pandemic is a global health crisis with over two hundred million infections and over four million deaths to date. Patients with acute respiratory distress due to SARS-CoV-2 infection exhibit a significantly weakened immune system. The degraded immune system is characterized by the hyper-inflammatory response and Type 1 Interferon (IFN-1) deficiency. In this study, we analyzed how NSP15 of SARS-CoV-2 can bind with human ubiquitin ligase RNF41 and interfere with and suppress the immune system, at a molecular level. Such an understanding will help in the challenging task of developing antiviral therapeutics against SARS-CoV-2.

## **Introduction**

SARS-CoV-2 is a highly transmissible coronavirus that emerged in late 2019 and has caused a global pandemic of COVID-19, a deadly respiratory disease. Research has indicated that SARS-CoV-2 invades cells through spike proteins and virus replication happens inside infected cells. Infected cells of critical patients with acute respiratory distress due to COVID-19 exhibit erratic human immune responses: hyper-inflammatory response and Type 1 Interferon deficiency (1-5). Hyper-inflammatory response damages healthy cells and tissues and is caused by chronic stimulation of the NF- $\kappa$ B immune signaling pathway. Type 1 Interferon deficiency is caused by underactive stimulation of the Type 1 Interferon signaling pathway. It prevents the suppression of viral replication in infected cells.

Human E3 Ubiquitin ligase, RNF41, plays a crucial role in modulating the immune system by negatively regulating the NF- $\kappa$ B signaling pathway and positively regulating the Type 1 Interferon signaling pathway (6-12). In an uninfected cell, Ubiquitin-specific protease 8, USP8, binds to the C-terminal domain of RNF41 (6-8,12-14). The binding between RNF41 and USP8 is disrupted when RNF41 is activated to bind to MYD88 in order to negatively regulate the NF- $\kappa$ B signaling pathway (7, 9, 12, 14) and positively regulate Type1 Interferon signaling pathway by binding to TBK1, a protein kinase (7, 9,12-15). Since RNF41 plays an important role in controlling the human immune signaling pathways that control the hyper-inflammatory response and Type 1 Interferon responses, RNF41 is an intriguing target to analyze in the context of SARS-CoV-2 infection. However, few research studies are available that investigate if RNF41's functions are affected by SARS-CoV-2 proteins.

A recent study has shown that SARS-CoV-2 NSP15, a nonstructural protein, decreases the human immune response and increases the rate of viral replication (16-19). However, the exact mechanism(s) by which NSP15 interferes with the human immune system have not been investigated at a molecular level (17, 20). Since RNF41 regulates the NF- $\kappa$ B and Type 1 Interferon immune signaling pathways to control the human immune response and reduce the rate of viral replication, whereas SARS-CoV-2 NSP15 degrades the human immune response and increases the rate of viral replication, we wanted to study if SARS-CoV-2 NSP15 can bind to RNF41 and inhibit the normal functions of RNF41 of regulating the NF- $\kappa$ B and Type 1 Interferon immune signaling pathways, as shown in Figure S1 in the supporting material.

## **Materials and Methods**

### **Analyzing the protein structures**

The sequences for RNF41, USP8, MYD88, TBK1, and SARS-CoV-2 NSP15 were downloaded from UniProt. The crystallized molecular protein structures downloaded

from Protein Data Bank (PDB) were RNF41 (PDB Code: 2GWF), MYD88 (PDB Code: 2Z5V), USP8 (PDB Code: 2GWF), TBK1 (PDB Code: 4IWO), and SARS-CoV2 NSP15. The sequences from UniProt were compared with PDB structures to detect if the entire sequences of the biomolecules were crystallized.

### Generating the structure of RNF41 ZFD

Only the crystallized structure of the RNF41 CTD was available in the PDB while the other domains were unavailable. SWISS-MODEL was used to create the RNF41 ZFD structure based on the RNF41 sequence downloaded from UniProt (UniProt Code: Q9H4P4). RNF41 ZFD structure is shown in Figure S2 in the supporting material.

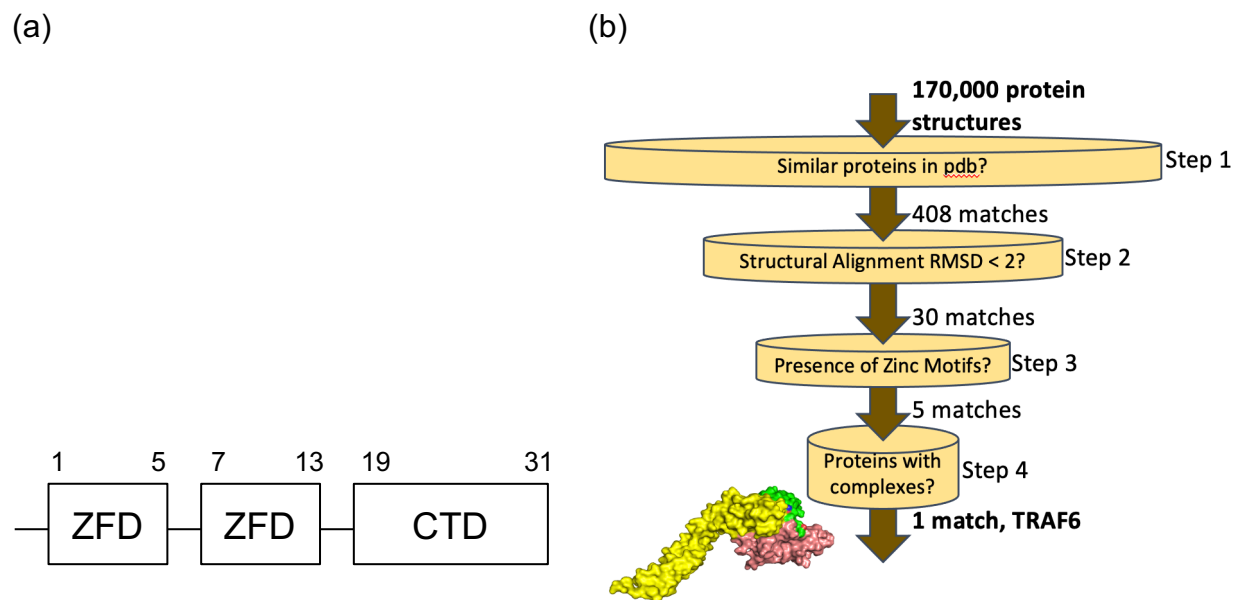


**Figure 1a: Domain arrangement of RNF41 and workflow of identifying RNF41 ZFD.**  
**(a).** RNF41 has 3 domains: zinc finger domain 1 (ZFD1), zinc finger domain 2 (ZFD2), and C-terminal domain (CTD). **(b)** Four steps to locate interaction surfaces on RNF41 ZFD out of 170,000 protein structures in PDB.

### Docking RNF41 CTD to USP8, MYD88, and TBK1

The following dockings were performed using HADDOCK (21, 22): USP8 to RNF41 CTD, MYD88 to RNF41 CTD, TBK1 to RNF41 CTD. Gly215, Met217, Thr220, Asp222, Glu252, Arg265, Arg269, and His312 were chosen as the active residues of RNF41 CTD for binding (8). CASTp (23), a protein-cavity detection software, was used to find possible interaction surfaces of MYD88, TBK1, and USP8. Glu44, Glu52, Lys95, and Leu96 were chosen as the residues for the MYD88 TIR domain for docking (24, 25). Ala237, His238, Asp241, Asp242, and Lys244 were chosen as the residues for USP8

for docking (8). Val79, Tyr108, Thr159, Ser172, Ser222, and Cys270 were chosen as the residues for TBK1 for docking.

### Docking NSP15 to RNF41 CTD

The residues of SARS-CoV-2 NSP15 that bind with another protein are unknown. So five different dockings to five different surfaces of NSP15 were performed as follows:

1. Docking pose 1: The residues chosen were His 236, His251, Lys291, Ser295, Trp342, and Tyr344. Most of the activity of cleaving leftover virus RNA after replication is performed in these sites (26-28). They lie on the C-terminal domain of NSP15.
2. Docking pose 2: The residues chosen were Ala219, Asp221, Phe223, Glu225, Tyr227, Glu235, Glu262, Pro264, Asp337, and His339. SARS-CoV NSP15's binding site with another protein was about 10 Å away from three of SARS-CoV NSP15's known sites which helped in the cleaving activity (27). 88% of the structure is conserved between SARS-CoV NSP15 and SARS-CoV-2 NSP15 (26). So, these sites were chosen. They lie on the C-terminal domain of NSP15.
3. Docking pose 3: The residues chosen were Val278, Val297, Val300, Val31, Phe304, Ile307, Ile308, Ile324, and Thr327. CASTp determined these as possible interaction surfaces on the C-terminal domain of NSP15.
4. Docking pose 4: The residues chosen were Ile65, Trp88, Asp89, Ala94, Ser105, Phe125, Ile145, Ser156, Ile170, and Gln189. CASTp determined these as possible interaction surfaces on the middle domain of NSP15.
5. Docking pose 5: The residues chosen were Asn66, Phe17, Gly19, Gln21, Val12, Lys36, Asp38, Glu43, Glu58, and Lys62. CASTp determined these as possible interaction surfaces on the N-terminal domain of NSP15.

### Docking NSP15 to RNF41 ZFD

There was no literature or crystallized structure in PDB that could be used to determine the interaction surfaces of RNF41 ZFD. So, it was decided to locate proteins that are structurally similar to RNF41 ZFD and then look for structures they complex with, to determine the interaction surfaces on RNF41 ZFD. The method used is explained as a sequence of steps below and shown in Figure 2:

1. Dali search (29) was used to search for structurally similar proteins to RNF41 ZFD in the PDB. Dali returned 408 matching proteins out of 170,000 structures in the PDB.
2. A python program was developed which performed the following steps to find zinc domains on the proteins returned by Dali:
  - a. For each protein returned by Dali, the program determined the chain from the PDB structure that matched the Dali result and created a list of these protein chains.
  - b. The program iterated through each protein chain and aligned it with RNF41 ZFD using PyMOL's align command and the Root Mean Square

- Deviation (RMSD) was saved. RMSD is a measure of the average distance between the atoms of the superimposed proteins.
- c. The program then filtered the proteins that had RMSD < 2 Å.
  - d. For proteins found in step c, the program checked if the structure contained a zinc atom or a ZFD by checking the sequence. ZFD was determined manually by searching for a set of two cysteine and two histidine residues with a short beta-hairpin and an alpha helix (beta/beta/alpha structure) between the Cys-Cys and His-His residues. JPred server (30) was used to manually detect beta hairpins and alpha-helix between the residues. This resulted in 5 proteins.
3. Subsequently, for each of the 5 proteins, the PDB was manually checked to determine if their crystallized complex with another protein was available. This resulted in only 1 protein, TRAF6 (PDB Code: 5VNZ), an E3 ligase, in complex with E2 ubiquitin-conjugating enzyme UBC13 and ubiquitin. RMSD of all atoms between RNF41 ZFD and TRAF6 was 0.15 Å and superimposed structures are shown in Figure S3. The location of the interaction surfaces of TRAF6 with UBC13 and ubiquitin (31) were used as the interaction surfaces for RNF41 ZFD.

Based on the above method, the interaction surfaces for RNF41 ZFD were determined as Ser58, Pro67, Arg70, Pro72, Arg73, Met75, Asp105, Glu107, Asn109, and Pro110. Five different docking simulations were performed using 5 different interaction surfaces of NSP15 determined earlier.

In all the dockings, the option to automatically select passive residues and to select all surface residues within a 3 Å radius around the active residues was specified in HADDOCK to allow for more surface coverage while docking. The binding scores (HADDOCK score) were recorded and the distances between the binding residues were measured using PyMOL.

### **Molecular Dynamics Simulations of the docked structure of NSP15 and RNF41**

For determining the dynamic stability of the NSP15 and RNF41 docked structure, molecular dynamics (MD) studies were performed using GROMACS (32) for 10 ns, at 300K, a water box with 10 Å, using OPLS/AA force field under the NPT ensemble with a time step of two femtoseconds (fs).

## **Results**

The HADDOCK output was analyzed based on the HADDOCK score and the number of members in the cluster. HADDOCK score consists of a linear combination of various energies and buried surface area (21, 22). A lower HADDOCK score signifies better binding. HADDOCK also takes the different combinations of the different complexes while it builds them and ranks or further organizes/clusters them based on structural

similarity (21, 22). A higher number of members of a cluster signifies a better cluster as it signifies that many complexes in the cluster have structural similarities (22).

### **Docking results of USP8 to the RNF41 CTD**

The best docked structure's HADDOCK score for USP8 and RNF 41 docking was -75.8 +/- 6.6 with 18 members as part of this cluster. USP8 bound to all 8 known interaction surfaces of RNF41 CTD at the residues at Gly215, Met217, Thr220, Asp222, Glu252, Arg265, Arg269, and His312. This is shown in Figure S4. The distances between the atoms ranged from 2.6 Å to 3.5 Å and the list of residues involved in the binding are shown in Table S1.

### **Docking results of MYD88 to the RNF41 CTD**

The best docked structure's HADDOCK score for MYD88 and RNF41 CTD docking was -72.9 +/- 10.6 with 12 members as part of this cluster. MYD88 bound to 5 out of the 8 known interaction surfaces of RNF41 CTD at the residues Met217, Glu252, Arg265, Arg269, and His312. This is shown in Figure S5. The distances between the atoms ranged from 2.8 Å to 4.0 Å and the list of residues involved in the binding are shown in Table S2.

### **Docking results of TBK1 to the RNF41 CTD**

The best docked structure's HADDOCK score for TBK1 and RNF 41 docking was -75.0 +/- 8.8 with 14 members as part of this cluster. TBK1 bound to 6 of 8 interaction surfaces on RNF41 CTD at the residues GLY-215, MET-217, THR-220, ASP-222, and HIS-312. This is shown in Figure S6. The distances between the atoms ranged from 2.6 Å to 3.8 Å and the list of residues involved in the binding are shown in Table S3.

### **Docking results of NSP15 to the RNF41 CTD**

The results of the five dockings of different poses of NSP15 to RNF41 CTD are shown in Table S4. The results of docking pose two of SARS-CoV-2 NSP15 and RNF41 CTD had the best HADDOCK score of -110.9 +/- 3.6 with 15 members as part of this cluster. In this docking, NSP15 bound to 6 of the 8 interaction surfaces of RNF41 CTD at the residues Met217, Thr220, Asp222, Glu252, Arg269, and His312. This docking is shown in Figure 3. The distances between the atoms ranged from 1.8 Å to 4.1 Å and the list of residues involved in the binding are shown in Table S5. Also, NSP15's residues that bound during docking number two were Asp221, Glu235, Ser243, His244, Arg259, Glu262, Lys336, and Glu341. These sites are different from NSP15's sites His236, His251, Lys291, Ser295, Trp342, and Tyr344 where cleaving leftover virus RNA is performed.

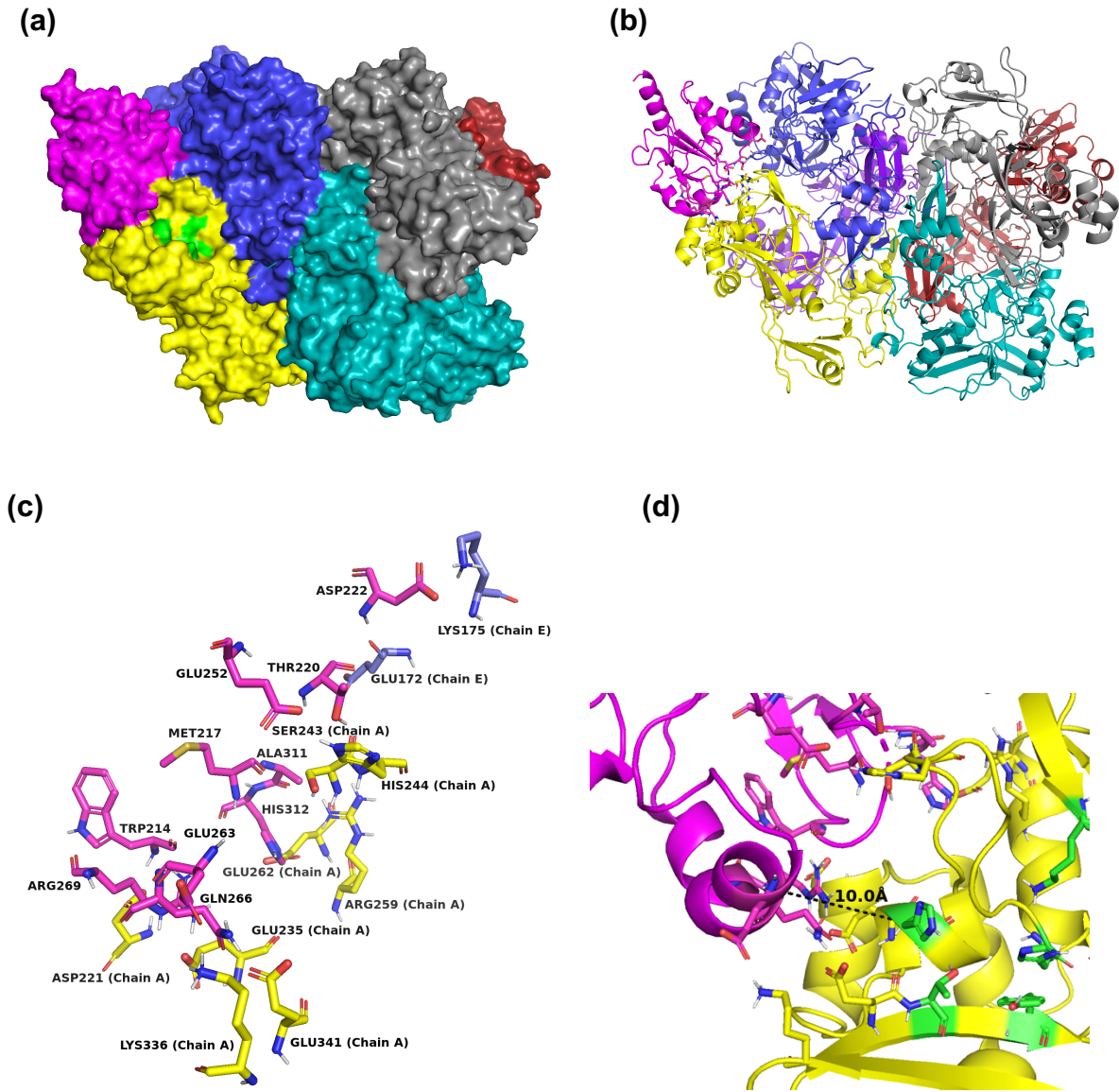


**Figure 3:** (a) Surface representation of the structure of SARS-CoV-2 NSP15 (Chain A: yellow, Chain B: teal, Chain D: firebrick, Chain E: light blue, Chain F: gray, Chain C: not visible) and RNF41 CTD (magenta) complex after the docking procedure. The green color on the surface represents the location where the cleaving activity of leftover RNA is performed by NSP15. (b) The Cartoon representation of the structure of SARS-CoV-2 NSP15 (Chain A: yellow, Chain B: teal, Chain C: purple, Chains D: firebrick, Chain E: light blue, Chain F: gray,) and RNF41 CTD (magenta) complex after the docking procedure showing the residues (in the respective chain colors) involved in the binding. (c) Stick representation of only the residues of SARS-CoV-2 NSP15 (Chain A = yellow and Chain E = light blue) and RNF41 CTD (magenta) involved in the binding. The hydrogen bonds are shown as dotted green lines. (d) Minimum distance between the C $\alpha$  atom of a residue of RNF41 CTD which participates in binding with NSP15 and the C $\alpha$  atom of a residue which is one of the sites where the cleaving activity of leftover RNA is performed by NSP15 was measured as 10.0 Å.

## Docking results of RNF41 ZFD to NSP15

The results of the five dockings of different poses of NSP15 to RNF41 ZFD are shown in Table S6. The results of docking pose one of SARS-CoV-2 NSP15 and RNF41 ZFD had the best HADDOCK score of -64.4 +/- 7.0 with 12 members as part of this cluster. The docking result of pose one is shown in Figure S7. The distances between the atoms ranged from 1.8 Å to 4.1 Å and the list of residues involved in the binding are shown in Table S7. The interaction surfaces for docking 1 of NSP15 are His236, His244, Trp334, Cys335, Lys336, Asp337, Glu341, Thr342, and Tyr344. Out of these sites, three sites His236, Thr342, and Tyr344 are the sites where most of the activity of cleaving leftover virus RNA after replication is performed by NSP15.

## Results of Molecular Dynamics simulations

Prior to performing the MD simulations on the docking of pose 2 of NSP15 and RNF41 CTD, energy minimization was performed. These results are shown in Figure S8. Subsequently, MD simulations were performed to determine if the docked structure was stable. RMSD plots of backbone atoms of the docked structure indicate it reaches stability after 7 ns. RMSD at equilibrium is ~5.1 Å as seen in Figure 4.

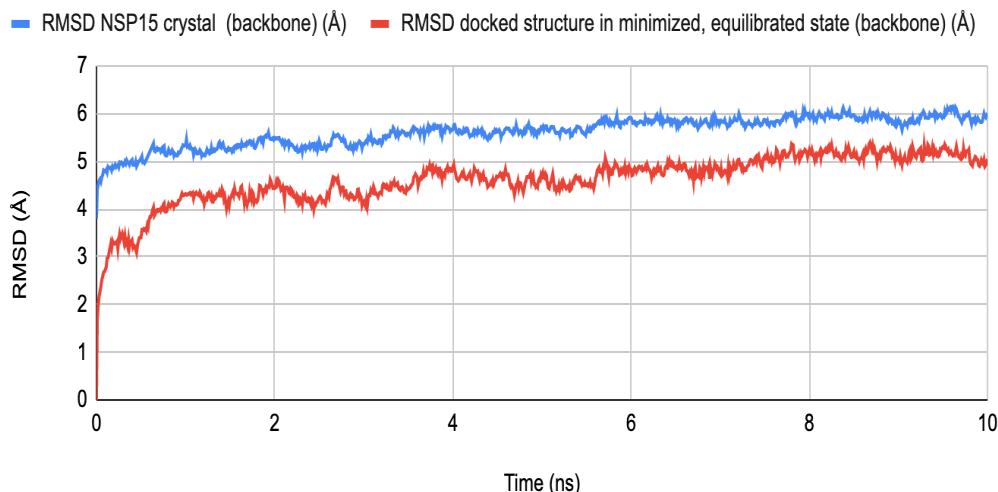


**Figure 4: MD simulation results of the RMSD of the backbone of NSP15 docked to RNF41 CTD**

The dynamic behavior of individual amino acid residues for RNF41 and NSP15 was determined in terms of Root Mean Square Fluctuations (RMSF). RMSF plots indicated RNF41 and NSP15 have an average RMSF of 0.64 Å and 0.96 Å respectively. The RNF41 residues Met217, Thr220, Asp222, Glu252, Arg269, and His312 involved in binding exhibited lower than average fluctuations (RMSF value). The 6 residues of NSP15 involved in the binding were Glu262, Glu235, Ser243, and His244 of one chain, Glu172 and Lys175 of a neighboring chain. Four out of the six residues exhibited

fluctuations either closer to or lower than average fluctuations (RMSF value). Two residues, Ser243 and His244, exhibited RMSF values of 1.11 Å and 0.94 Å respectively which is greater than the average RMSF of 0.96 Å. This indicated slightly lesser stability for these two residues in the interaction. RMSF of the backbone of the docked structure for RNF41 CTD and NSP15 residues are shown in Figures S9 (a) and (b) respectively.

## Discussion

HADDOCK docking results of USP8 and RNF41 CTD were the same as the crystallization results as described by Avvakumov et al (8). This verified the choice of HADDOCK as a good docking server for this project. The binding results consisting of the HADDOCK score and distances between the residues indicate a good binding affinity.

The dockings of MYD88 to RNF41 CTD and TBK1 to RNF41 CTD using HADDOCK confirmed that MYD88 and TBK1 bind to the RNF41 CTD. The HADDOCK score and distances between the residues indicate a good binding affinity. Their docking results are comparable to that of USP8 and RNF41 CTD.

Of the different dockings of five poses of NSP15 and RNF41 CTD, docking of pose number 2 of NSP15 to RNF41 CTD has the best binding results. The HADDOCK score and distances between the residues indicate a good binding affinity. In this docking, NSP15 docked to 6 out of the 8 interaction surfaces of RNF41 with distances  $\leq$  4.1 Å. The binding between NSP15 and RNF41 happened across two chains of NSP15, chain A and Chain E. Also, NSP15's residues that bound during docking number two to RNF41 were at least 10.0 Å away from NSP15's sites of His236, His251, Lys291, Ser295, Trp342, and Tyr344 where most of the activity of cleaving leftover virus RNA after replication is performed.

The structure of the zinc finger domains of RNF41 was previously unpublished, so it was created using homology modeling. Binding NSP15 to RNF41 ZFD was performed in order to test if NSP15 had better binding metrics with the zinc finger domains of RNF41 compared to RNF41 CTD. Since there was no literature or crystallized structure in the PDB that can be used to determine the interaction surfaces in the Zinc Fingers of RNF41, interaction surfaces on structurally similar proteins were determined using DALI search, PyMOL alignment, and presence of zinc motifs. The guiding principle behind this approach was that locating proteins that are structurally similar to the zinc finger domains of RNF41 and then looking for structures they complex with, can help in locating the interaction surfaces on the zinc fingers of RNF41. A 3D structural search of 170,000 entries in the PDB resulted in 408 proteins, matching proteins which were further filtered to only 1 protein, TRAF6, using software developed to perform structural alignment and zinc motif filtration. TRAF6 like RNF41 is an E3 ligase which verifies the structure of the zinc fingers of RNF41 using homology modeling. Also, aligning RNF41 ZFD and TRAF6 resulted in a RMSD of 0.15 Å, which indicated excellent structural similarity.

The crystallized structure of TRAF6 in complex with E2 Ubiquitin-conjugating enzyme UBC13 and Ubiquitin is available in the PDB. Due to the similarity in the structure and function of TRAF6 and zinc finger domains of RNF41, the binding residues found of TRAF6, UBC13, and can be used as the binding residues of the zinc fingers domains of RNF41. Five different dockings were performed using the same 5 different sets of binding residues on NSP15 to bind to the zinc finger domains of RNF41 and the binding metrics were compared to check for the best residues on NSP15 that can bind to RNF41 ZFD. Docking number 1 had the best binding metrics with the lowest binding energy of -64.4 +/- 7.0 which indicated a good binding affinity.

**Table 1: Comparing the best docking results of NSP15 to RNF41 ZFD and NSP15 to RNF41 CTD**

Type of Complex	HADDOCK Score (Binding energy)	Number of Members in the cluster chosen
Docking pose 1 of NSP15 to RNF41 ZFD	-64.4 +/- 7.0	12
Docking 2 of NSP15 to RNF41 CTD	-110.9 +/- 3.6	13

Docking 2 of NSP15 to the RNF41 CTD had a much lower binding energy (HADDOCK score) value of -110.9 +/- 3.6 than the binding energy of docking 1 of NSP15 to RNF41 ZFD whose value is -64.4 +/- 7.0. The number of members in the cluster in docking 2 of NSP15 to the RNF41 CTD had better values than docking 1 of NSP15 to RNF41 ZFD. So, docking 2 of NSP15 to the RNF41 CTD had overall better binding metrics than docking 1 of NSP15 to RNF41 ZFD. Therefore, in the presence of both the CTD and the ZFD of RNF41, NSP15 will have a greater affinity to bind to RNF41 CTD. Also, in the docking of NSP15 to RNF41 ZFD, three residues of NSP15 involved in the binding, are His236, Thr342, and Tyr344, are part of the 6 residues where most of the activity of cleaving leftover virus RNA after replication happens. The interaction surfaces of NSP15 to RNF41 CTD were at least 10.0 Å away from the sites on NSP15 where the cleaving activity takes place on NSP15.

USP8, MYD88, TBK1, and NSP15 all bind to most of the interaction surfaces of RNF41 CTD as shown in Table S8 and have good binding metrics. RNF41 CTD had the best binding metrics with NSP15 than with USP8, TBK1, and MYD88.

RNF41 plays an important role in negatively regulating the NF-κB human immune signaling pathway (6-12). MYD88 stimulates the NF-κB pathway to produce cytokines in response to the presence of foreign pathogens (12). In the presence of excessive cytokines, RNF41 is activated, and it binds to MYD88 and polyubiquitinates it with K48.

This signals MYD88 for degradation. If NSP15 binds to the interaction surfaces of RNF41, then RNF41 may not be unable to bind to MyD88 and negatively regulate the NF- $\kappa$ B human immune signaling pathway. This can lead to uncontrolled production of cytokines which can cause excessive inflammation and can damage healthy cells and tissues. Hyper-inflammation is seen as one of the major causes of disease severity and death in SARS-CoV2 infection (1-5). RNF41 also plays an important role in positively regulating the Type 1 Interferon human immune signaling pathway. In response to the presence of foreign pathogens, RNF41 binds to the protein kinase TBK1 and polyubiquitinates it with K63 (12). This stimulates the production of Type 1 Interferons which are responsible for inhibiting viral replication by activating various immune cells to fight the viral infection. If NSP15 binds to the interaction surfaces of RNF41, then RNF41 may not be unable to bind to TBK1 to stimulate the production of Type 1 Interferons. Reduced levels of Type 1 Interferons are seen in severe SARS-CoV2 infections (1-5).

The residues of SARS CoV2 NSP15 that bind to RNF41 CTD are at least 10.0 Å away from NSP15's sites where most of the activity of cleaving leftover virus RNA after replication is performed. So, when NSP15 binds to the interaction surfaces of RNF41, NSP15 can also continue its function of cleaving leftover virus RNA. The residues of NSP15 that bind to the interaction surfaces of RNF41 are Glu235, Ser243, His244, and Glu262 on Chain A and Glu172 and Lys175 on Chain E. These sites of NSP15 can be used as a target by drugs to inhibit NSP15 from binding to RNF41.

## Conclusion

In this ongoing COVID-19 pandemic, *in silico* methodologies can be used to accelerate the process of understanding the binding interactions of SARS-CoV-2 with human proteins at an atomic level. In this study, we used homology modeling, molecular docking, molecular dynamics, and developed a Python program to confirm our hypothesis that SARS-CoV-2 NSP15 can bind to human RNF41 and inhibit RNF41 from performing its function of regulating the NF- $\kappa$ B and Type 1 Interferon immune signaling pathways. The strength and the stability of the binding between SARS-CoV2 NSP15 and human RNF41 were evaluated using HADDOCK metrics and by analyzing the results of the MD simulations respectively. The results of our work on binding interactions between the RNF41 and SARS-CoV-2 NSP15 would be useful for further studies, including the design of efficient antiviral agents to target NSP15.

## Acknowledgments

This project is partially funded by the Department of Energy's National Virtual Biotechnology Laboratory. The authors are grateful to Dr. Joao Rodriguez, Stanford University, currently in Schrödinger, for the guidance on using HADDOCK.

## Supplementary materials

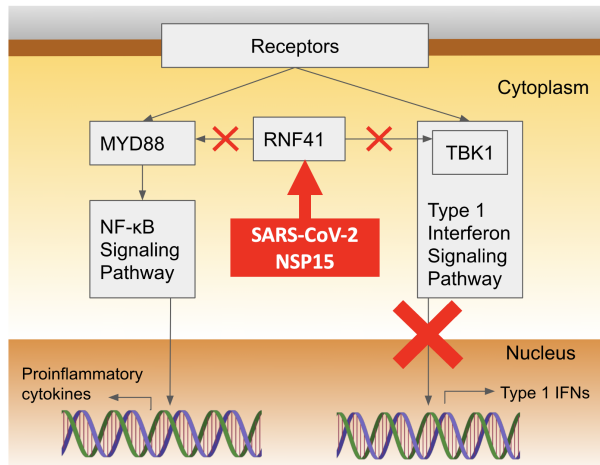


**Figure S1: Potential disruption of NF- $\kappa$ B and Type 1 Interferon Signaling Pathways in host cells infected with SARS-CoV-2 virus**

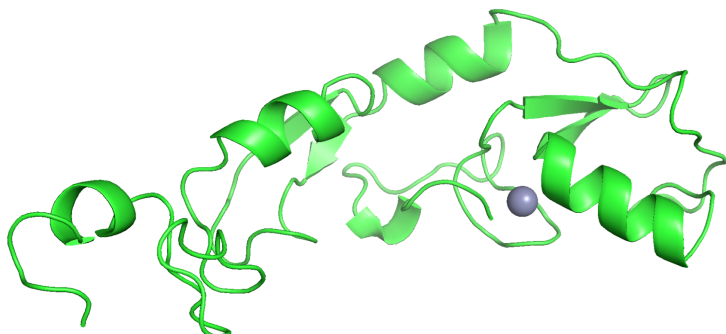


**Figure S2: 3D ribbon structure of RNF41 ZFDs (green) generated using SWISS-MODEL. The zinc atom is shown as a purple sphere.**

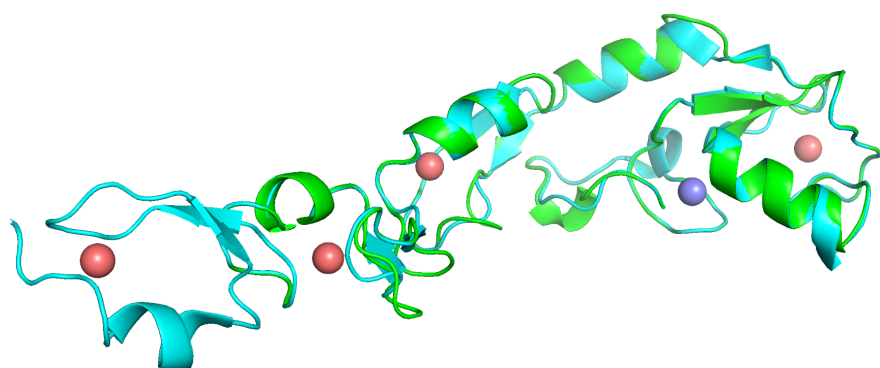


**Figure S3: 3D Ribbon structure of the alignment of RNF41 ZFDs (green) and TRAF6 (cyan). TRAF6 has 5 zinc atoms while RNF41 ZFD has 1 zinc atom. The zinc atom of RNF41 ZFD overlaps with one of the zinc atoms (Zn301 in PDB 5VO0)**

of TRAF6 and is shown as a purple sphere. The zinc atoms of only TRAF6 are shown as salmon spheres.

**Table S1: Interactions between RNF41 CTD and USP8.**

RNF41 CTD	USP8	Distances (Å)	Bond Type
Arg265 NE	Asp241 OD2	2.7	Ionic
Arg269 NH2	Asp242 OD1	2.6	Ionic
Glu252 OE1	Lys244 HZ2	2.6	Ionic
Thr220 OG1	Ala237 O	2.7	H-bond
Gln266 NE2	Asp242 OD1	3.4	H-bond
Met217 O	Asp241 N	2.7	H-bond
Gly215 O	Asp242 N	3.2	H-bond
His312 NE2	Gln211 OE1	3.5	H-bond
Asp222 OD2	His238 NE2	3.2	H-bond
Arg265 NH2	Asp241 OD1	2.7	Ionic

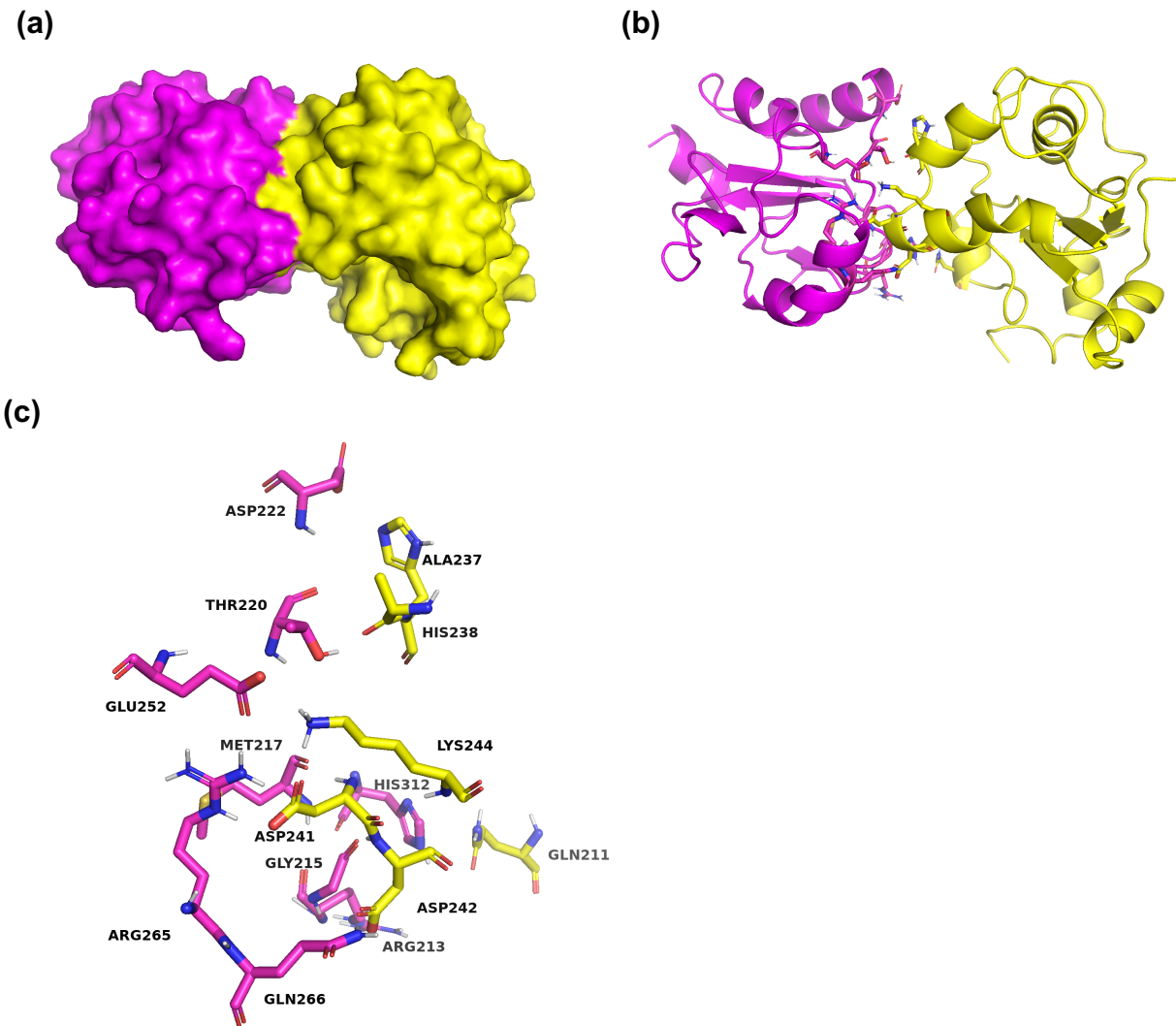


**Figure S4:** (a) Surface representation of the structure of USP8 (yellow) - RNF41 CTD (magenta) complex after the docking procedure. (b) Cartoon representation of the structure of USP8 (yellow) - RNF41 CTD (magenta) complex after the docking procedure showing the residues (in the respective chain colors) involved in the binding. (c) Close-up of the stick representation of the known active binding sites of RNF41 (magenta) and the residues of USP8 (yellow) that bind to it.

**Table S2: Interactions between RNF41 CTD and MYD88.**

<b>RNF41 CTD</b>	<b>MYD88</b>	<b>Distances (Å)</b>	<b>Bond Type</b>
ARG269 NH1	GLU52 OE2	3.2	Ionic
ARG270 NE	GLU57 OE2	2.8	Ionic
ARG213 NH1	LEU96 O	2.9	H-bond
ARG213 NH2	LYS95 O	3.4	H-bond
ARG265 NH2	GLN42 OE1	2.8	H-bond
GLN266 NE2	GLU65 OE1	2.8	H-bond
GLU252 OE2	GLU42 NE2	2.9	H-bond
MET217 N	GLU42 O	3.2	H-bond
HIS312 NE2	LEU96 O	4.0	H-bond

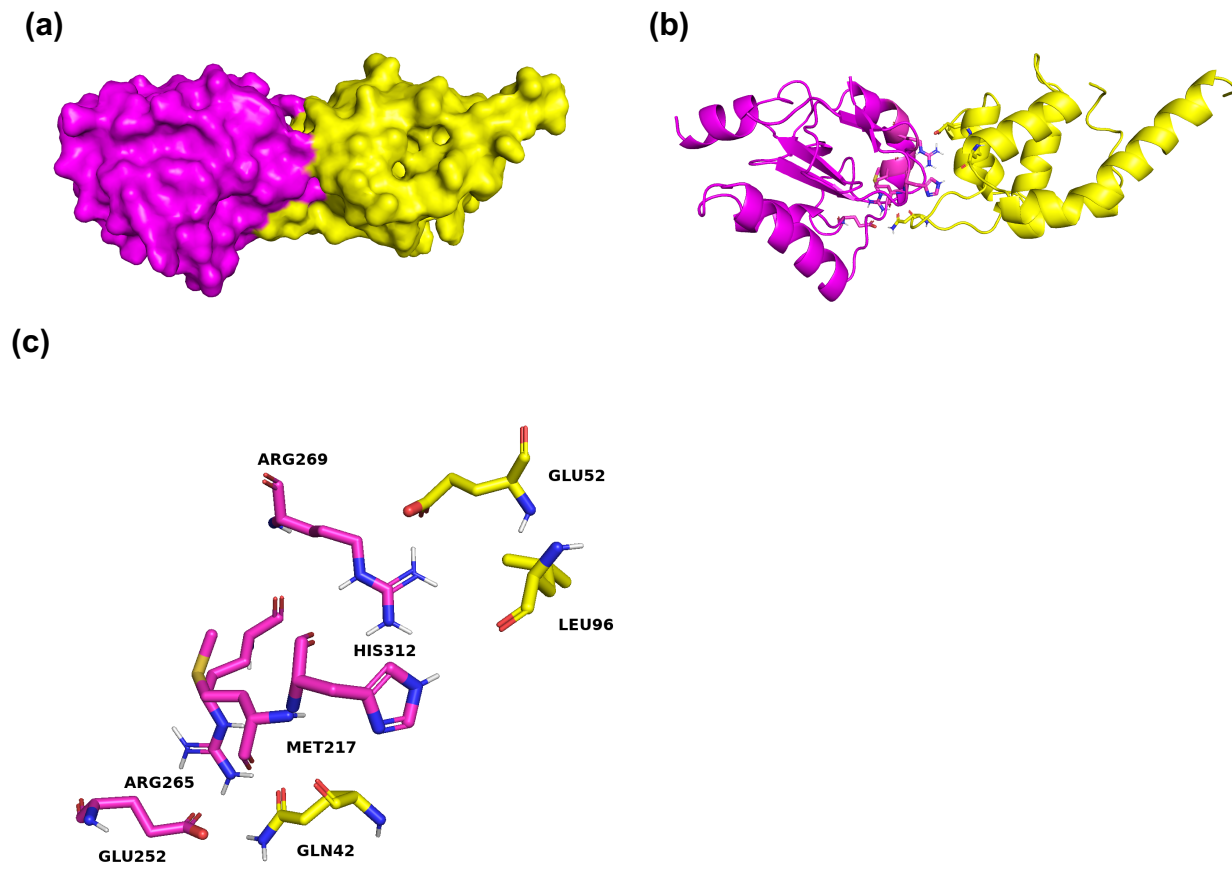


**Figure S5:** (a) Surface representation of the structure of MYD88 (yellow) - RNF41 CTD (magenta) complex after the docking procedure. (b) Cartoon representation of the structure of MYD88 (yellow) - RNF41 CTD (magenta) complex after the docking procedure showing the residues (in the respective chain colors) involved in the binding. (c) Close-up of the stick representation of the known active binding sites of RNF41 (magenta) and the residues of MYD88 (yellow) that bind to it.

**Table S3: Interactions between RNF41 CTD and TBK1.**

RNF41 CTD	TBK1	Distances (Å)	Bond Type
GLY215 O	THR333 OG1	2.7	H-bond
MET217 O	SER218 OG1	3.8	H-bond
SER219 OG	GLU219 NE2	2.8	H-bond
THR220 OG1	ASN330 ND2	2.7	H-bond
ASP222 OD2	LYS341 NZ	2.6	Ionic
HIS312 ND1	GLU337 OE1	2.6	H-bond

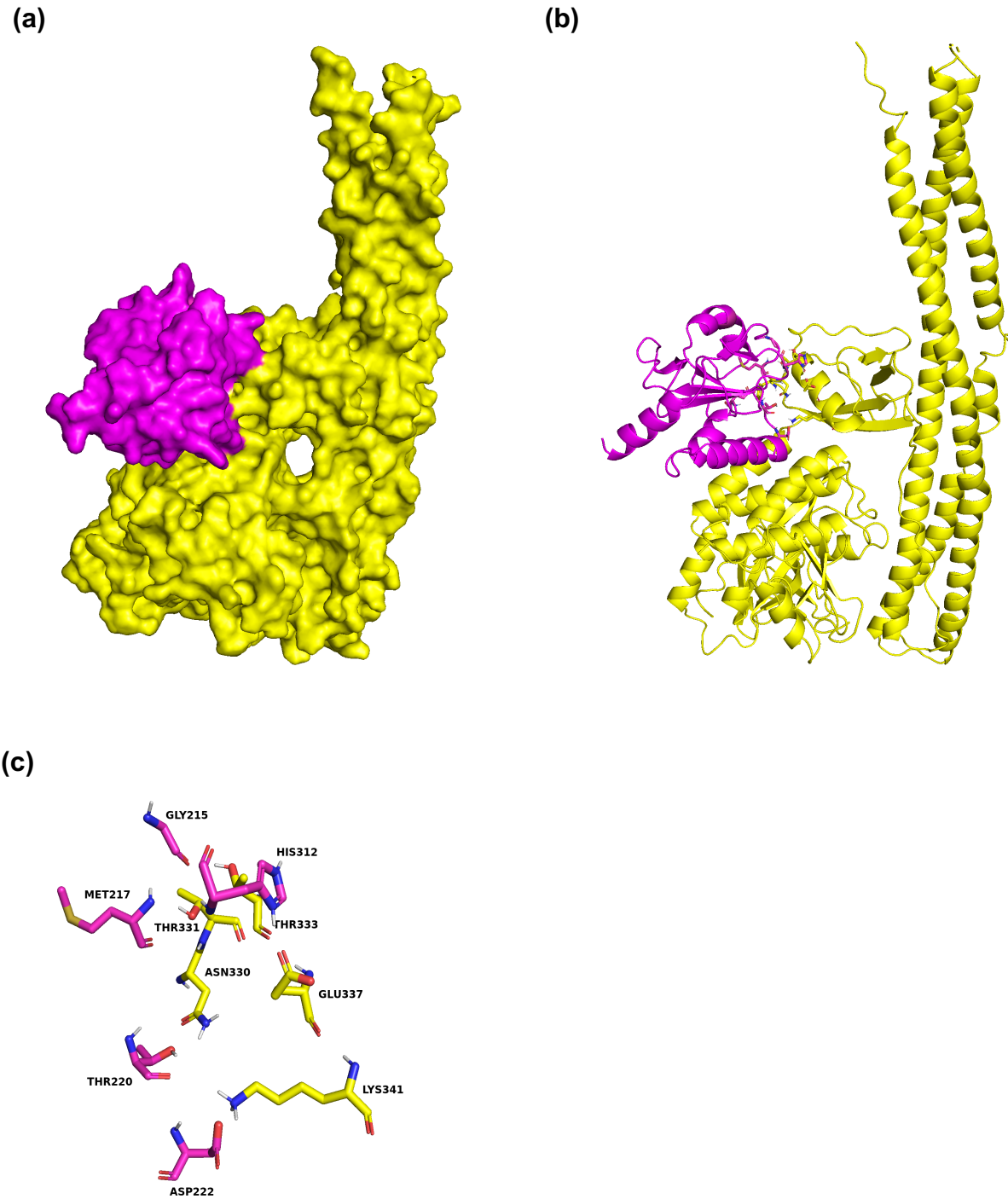


**Figure S6:** (a) Surface representation of the structure of TBK1 (yellow) - RNF41 CTD (magenta) complex after the docking procedure. The binding area is shown in green. (b) Cartoon representation of the structure of TBK1 (yellow) - RNF41 CTD (magenta) complex after the docking procedure showing the residues (in the respective chain colors) involved in the binding. (c) Close-up of the stick representation of the known active binding sites of RNF41 (magenta) and the residues of TBK1 (yellow) that bind to it.

**Table S4: Comparing results of 5 different dockings of NSP15 and RNF41 CTD**

Docking pose of NSP15	HADDOCK Score (Binding energy)	Number of members in the cluster	Number of binding sites of RNF41 that NSP15 binds to out of the total number of known active binding sites on RNF41
1	-91.4 +/- 9.0	12	5 out of 8
2	-110.9 +/- 3.6	15	6 out of 8
3	-79.6 +/- 5.6	5	3 out of 8
4	-40.4 +/- 2.0	4	0 out of 8
5	-29.4 +/- 10.1	4	0 out of 8

**Table S5: The list of residues involved in the binding of RNF41 CTD and docking pose 2 of SARS-CoV-2 NSP15 and the measured distances between them.**

RNF41 CTD (Residue Name, Residue Number, Atom Name)	NSP15 (Residue Name, Residue Number, Atom Name, chain name)	Distances (Å)	Bond Type
ASP222 OD2	LYS175 NZ (Chain E)	2.8	H-bond
ASP222 N	GLU172 O (Chain E)	2.8	H-bond
THR220 OG1	SER243 O (Chain A)	2.7	H-bond
GLU252 OE2	HIS244 NE2 (Chain A)	3.0	H-bond
ALA311 O	ARG259 NH1 (Chain A)	3.5	H-bond
HIS312 ND1	GLU262 OE1 (Chain A)	2.6	H-bond
HIS312 ND1	GLU262 OE2 (Chain A)	3.0	H-bond
GLN266 NE2	GLU341 OE1 (Chain A)	2.8	H-bond
GLU263 OE1	LYS336 NZ (Chain A)	2.6	H-bond
ARG269 NH2	GLU235 OE2 (Chain A)	2.7	H-bond
ARG269 NE	GLU235 OE2 (Chain A)	3.0	H-bond
TRP214 N	ASP221 OD2 (Chain A)	2.8	H-bond
MET217 O	SER243 OG (Chain A)	4.1	H-bond

**Table S6: Comparing results of 5 different dockings of NSP15 and RNF41 ZFD**

Docking pose of NSP15	HADDOCK Score (Binding energy)	Number of members in the cluster
Docking pose1 of NSP15	-64.4 +/- 7.0	12
Docking pose 2 of NSP15	-50.5 +/- 9.1	8
Docking pose 3 of NSP15	-35.7 +/- 2.1	5
Docking pose 4 of NSP15	-38.4 +/- 6.0	6
Docking pose 5 of NSP15	-29.5 +/- 9.3	5

**Table S7: Interactions between RNF41 ZFD and SARS-CoV-2 NSP15 (docking pose 1)**

RNF41 ZFD	NSP15	Distances (Å)	Bond Type
ASN98 ND2	ASP337 OD2 (Chain A)	2.7	H-bond
ASP105 OD2	LYS336 NZ (Chain A)	2.6	H-bond
ASP105 OD1	CYS335 N (Chain A)	3.8	H-bond
GLU107 OE2	TRP334 NE1 (Chain A)	3.9	H-bond
ASP127 OD1	TYR344 OH (Chain A)	2.7	H-bond
GLU107 OE2	THR342 OG1 (Chain A)	2.7	Ionic
LEU138 N	GLN20 OE1 (Chain E)	3.2	H-bond
SER91 O	HIS244 NE2 (Chain A)	4.6	H-bond
SER91 O	HIS236 ND1 (Chain A)	4.0	H-bond
HIS102 NE2	GLU341 OE2 (Chain A)	4.3	H-bond

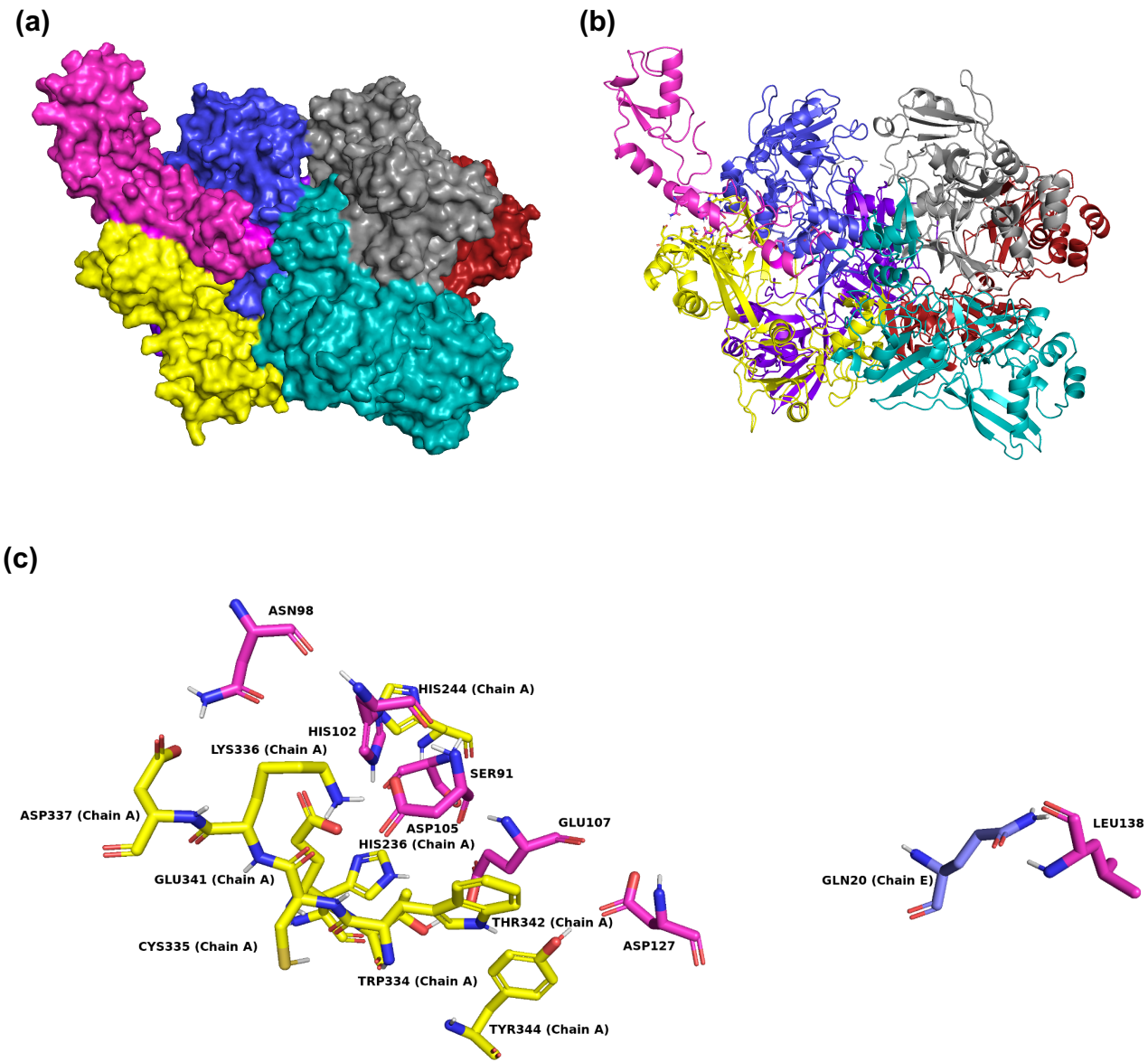


**Figure S7:** (a) Surface representation of the structure of SARS-CoV-2 NSP15 (Chain A: yellow, Chain B: teal, Chains D: firebrick, Chain E: light blue, Chain F: gray, Chain C: not visible) and RNF41 ZFD (magenta) complex after the docking procedure. (b) Close-up of the Cartoon representation of the structure of SARS-CoV-2 NSP15 (Chain A: yellow, Chain B: teal, Chain C: purple, Chains D: firebrick, Chain E: light blue, Chain F: gray,) and RNF41 ZFD (magenta) complex after the docking procedure showing the residues (in the respective chain colors) involved in the binding. (c) Stick representation of only the residues of SARS-CoV-2 NSP15 (Chain A = yellow and Chain E = light blue) and RNF41 ZFD (magenta) involved in the binding.

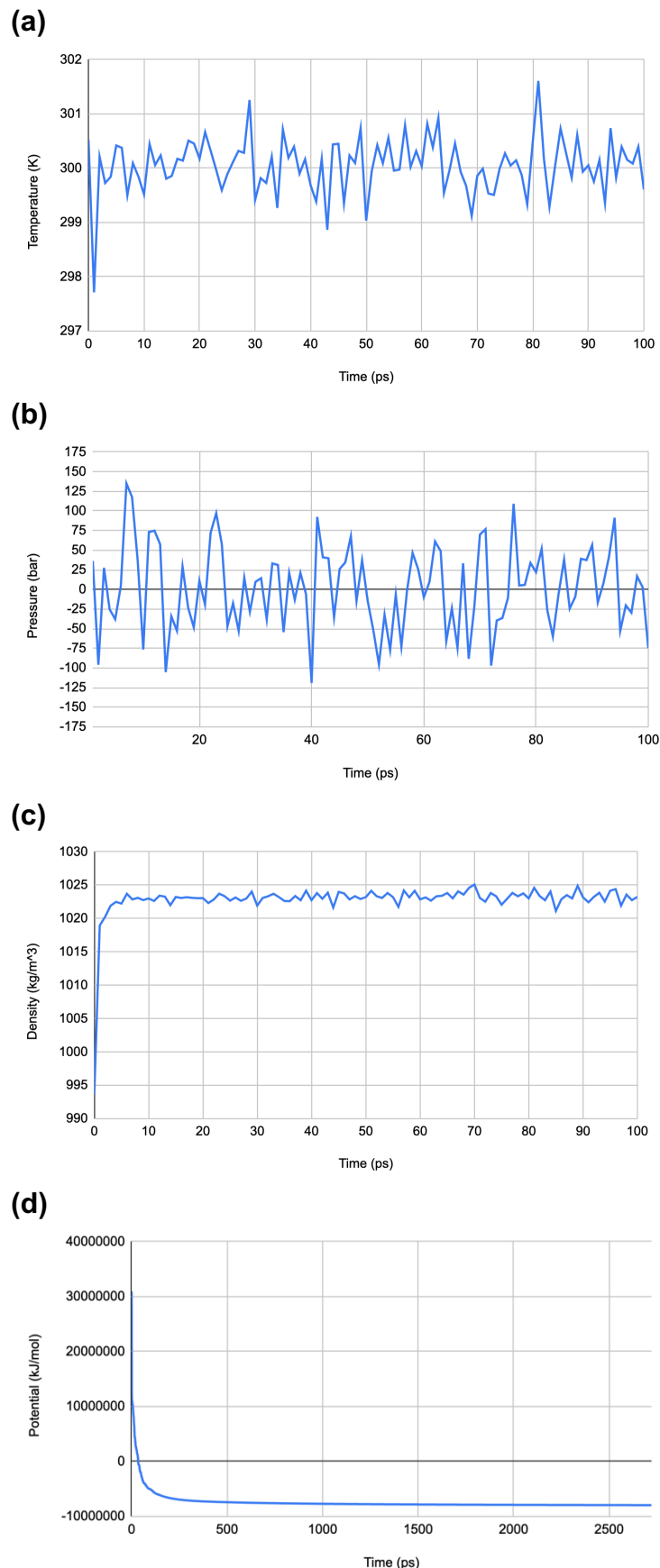


**Figure S8. Energy minimization results for MD simulations. a. Temperature. b. Pressure. c. Density, d. Potential Energy. The results indicate that the forces converge.**

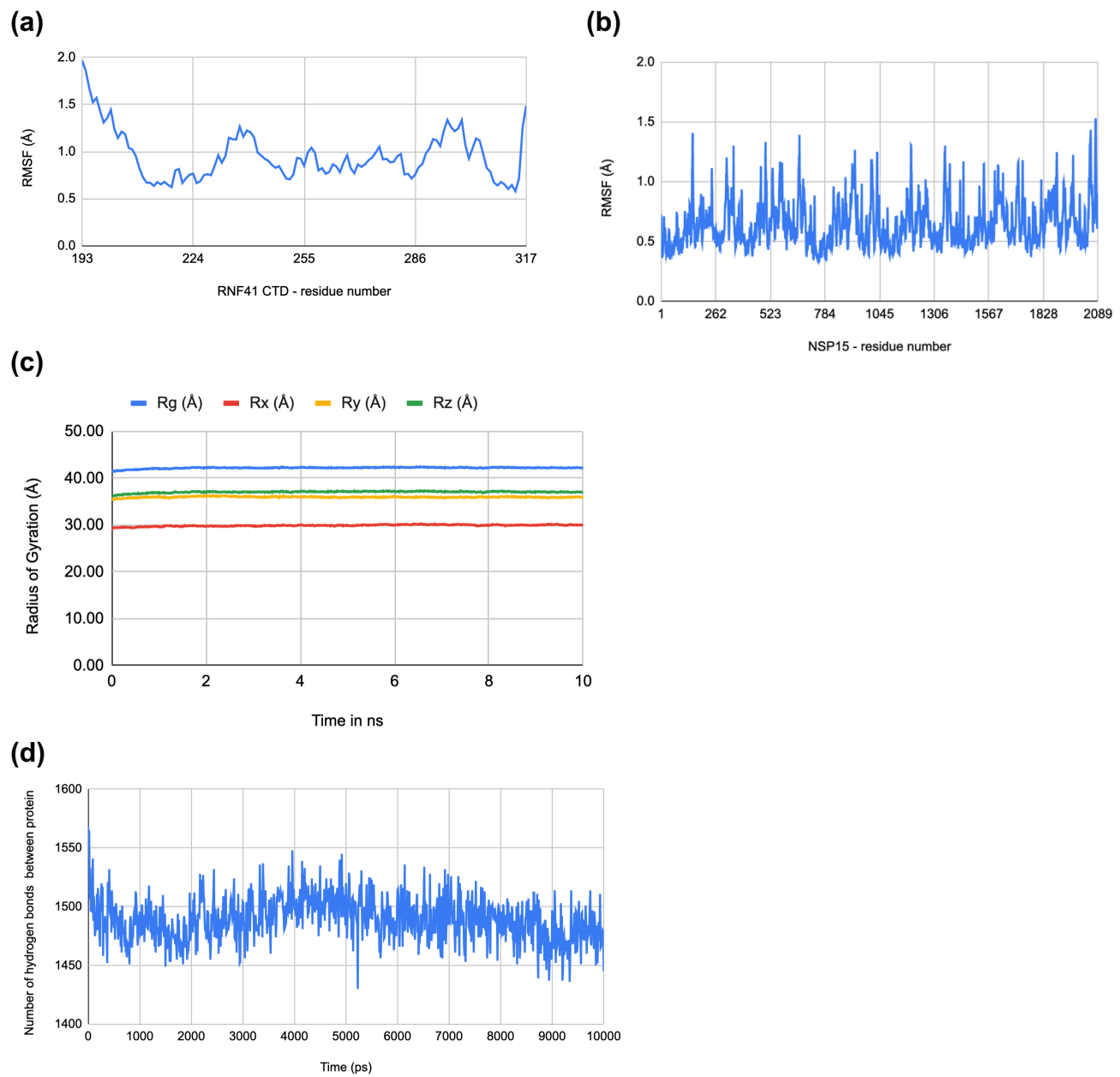


**Figure S9:** (a) RMSF of the backbone of the docked structure for RNF41 CTD residues (b) RMSF of the backbone of the docked structure for NSP15 residues (c) Rg of the backbone of NSP15 docked to RNF41 CTD. The radius of gyration (Rg) attained a constant value of ~42.0 Å after 2 ns which is close to the average value of 42.2 Å. (d) The total number of hydrogen bonds in the proteins. The average number of hydrogen bonds in the proteins was ~1480 and the donor-acceptor distances were less than 3.5 Å. The number of hydrogen bonds remains close to the average throughout the 10 ns period except at the beginning from t=0 ns to t=0.1 ns where the average number of hydrogen bonds in the proteins was ~1520 and the donor-acceptor distances were less than 3.5 Å.

**Table S8: Residues of RNF41 CTD that bind with USP8, TBK1, MYD88, and docking pose 2 of NSP15**

Proteins	Binding residues on RNF41							
	Gly215	Met217	Thr220	Asp222	Glu252	Arg265	Arg269	His312
<b>USP8</b>	yes	yes	yes	yes	yes	yes	yes	yes
<b>TBK1</b>	yes	yes	yes	yes	no	no	no	yes
<b>MYD88</b>	no	yes	no	no	yes	yes	yes	yes
<b>NSP15 (pose 2)</b>	no	yes	yes	yes	yes	no	yes	yes

## References

1. Sa Ribero, M., N. Jouvenet, M. Dreux, and S. Nisole. 2020. Interplay between SARS-CoV-2 and the type I interferon response. *PLOS Pathogens*. 16. <https://doi.org/10.1371/journal.ppat.1008737>
2. Yuen, C.-K., J.-Y. Lam, W.-M. Wong, L.-F. Mak, X. Wang, H. Chu, J.-P. Cai, D.-Y. Jin, K.K.-W. To, J.F.-W. Chan, K.-Y. Yuen, and K.-H. Kok. 2020. SARS-CoV-2 NSP13, NSP14, NSP15 and ORF6 function as potent interferon antagonists. *Emerging Microbes & Infections*. 9: 1418–1428. <https://doi.org/10.1080/22221751.2020.1780953>
3. Del Valle, D.M., S. Kim-Schulze, H.-H. Huang, N.D. Beckmann, S. Nirenberg, B. Wang, Y. Lavin, T.H. Swartz, D. Madduri, A. Stock, T.U. Marron, H. Xie, M. Patel, K. Tuballes, O. Van Oekelen, A. Rahman, P. Kovatch, J.A. Aberg, E. Schadt, S. Jagannath, M. Mazumdar, A.W. Charney, A. Firpo-Betancourt, D.R. Mendu, J. Jhang, D. Reich, K. Sigel, C. Cordon-Cardo, M. Feldmann, S. Parekh, M. Merad, and S. Gnjatic. 2020. An inflammatory cytokine signature predicts COVID-19 severity and survival. *Nature Medicine*. 26: 1636–1643. <https://doi.org/10.1038/s41591-020-1051-9>
4. Li, S., Y. Zhang, Z. Guan, H. Li, M. Ye, X. Chen, J. Shen, Y. Zhou, Z.-L. Shi, P. Zhou, and K. Peng. 2020. SARS-CoV-2 triggers inflammatory responses and cell death through caspase-8 activation. *Signal Transduction and Targeted Therapy*. 5. <https://doi.org/10.1038/s41392-020-00334-0>
5. Meffre, E., and A. Iwasaki. 2020. Interferon deficiency can lead to severe COVID. *Nature*. 587: 374–376. <https://doi.org/10.1038/d41586-020-03070-1>

6. Wu, X., L. Yen, L. Irwin, C. Sweeney, and K.L. Carraway. 2004. Stabilization of the E3 ubiquitin ligase NRDp1 by the deubiquitinating enzyme USP8. *Molecular and Cellular Biology*. 24: 7748–7757. <https://doi.org/10.1128/mcb.24.17.7748-7757.2004>
7. De Ceuninck, L., J. Wauman, D. Masschaele, F. Peelman, and J. Tavernier. 2013. Reciprocal cross-regulation between RNF41 and USP8 controls cytokine receptor sorting and processing. *Journal of Cell Science*. <https://doi.org/10.1242/jcs.131250>
8. Avvakumov, G.V., J.R. Walker, S. Xue, P.J. Finerty, F. Mackenzie, E.M. Newman, and S. Dhe-Paganon. 2006. Amino-terminal dimerization, NRDp1-rhodanese interaction, and inhibited catalytic domain conformation of the ubiquitin-specific protease 8 (USP8). *Journal of Biological Chemistry*. 281: 38061–38070. <https://doi.org/10.1074/jbc.m606704200>
9. Cohen, P., and S. Strickson. 2017. The role of hybrid ubiquitin chains in the myd88 and other innate immune signalling pathways. *Cell Death & Differentiation*. 24: 1153–1159. <https://doi.org/10.1038/cdd.2017.17>
10. Talreja, J., and L. Samavati. 2018. K63-linked polyubiquitination on TRAF6 regulates LPS-mediated MAPK activation, cytokine production, and bacterial clearance in toll-like receptor 7/8 primed murine macrophages. *Frontiers in Immunology*. 9. <https://doi.org/10.3389/fimmu.2018.00279>
11. Takaesu, G., R.M. Surabhi, K.-J. Park, J. Ninomiya-Tsuji, K. Matsumoto, and R.B. Gaynor. 2003. TAK1 is critical for IκB kinase-mediated activation of the NF-κB pathway. *Journal of Molecular Biology*. 326: 105–115. [https://doi.org/10.1016/S0022-2836\(02\)01404-3](https://doi.org/10.1016/S0022-2836(02)01404-3)
12. Zhang, Y., L.-F. Li, M. Munir, and H.-J. Qiu. 2018. Ring-domain E3 ligase-mediated host–virus interactions: Orchestrating immune responses by the host and antagonizing immune defense by viruses. *Frontiers in Immunology*. 9. <https://doi.org/10.3389/fimmu.2018.01083>
13. Zhang, X., A.H. Smits, G.B.A. van Tilburg, P.W.T.C. Jansen, M.M. Makowski, H. Ovaa, and M. Vermeulen. 2017. An interaction landscape of Ubiquitin signaling. *Molecular Cell*. 65. <https://doi.org/10.1016/j.molcel.2017.01.004>
14. Wauman, J., L. De Ceuninck, N. Vanderroost, S. Lievens, and J. Tavernier. 2011. RNF41 (NRDp1) controls type 1 cytokine receptor degradation and ectodomain shedding. *Journal of Cell Science*. 124: 921–932. <https://doi.org/10.1242/jcs.078055>
15. Wang, C., T. Chen, J. Zhang, M. Yang, N. Li, X. Xu, and X. Cao. 2009. The E3 ubiquitin ligase NRDp1 'preferentially' promotes TLR-mediated production of type I Interferon. *Nature Immunology*. 10: 744–752. <https://doi.org/10.1038/ni.1742>
16. Deng, X., and S.C. Baker. 2018. An “old” protein with a new story: Coronavirus endoribonuclease is important for evading host antiviral defenses. *Virology*. 517: 157–163. <https://doi.org/10.1016/j.virol.2017.12.024>
17. Ancar, R., Y. Li, E. Kindler, D.A. Cooper, M. Ransom, V. Thiel, S.R. Weiss, J.R. Hesselberth, and D.J. Barton. 2020. Physiologic RNA targets and refined

- sequence specificity of coronavirus endou. *RNA*. 26: 1976–1999.  
<https://doi.org/10.1101/2020.05.20.064436>
18. Kindler, E., C. Gil-Cruz, J. Spanier, Y. Li, J. Wilhelm, H.H. Rabouw, R. Züst, M. Hwang, P. V'kovski, H. Stalder, S. Marti, M. Habjan, L. Cervantes-Barragan, R. Elliot, N. Karl, C. Gaughan, F.J. van Kuppeveld, R.H. Silverman, M. Keller, B. Ludewig, C.C. Bergmann, J. Ziebuhr, S.R. Weiss, U. Kalinke, and V. Thiel. 2017. Early endonuclease-mediated evasion of RNA sensing ensures efficient coronavirus replication. *PLOS Pathogens*. 13. <https://doi.org/10.1371/journal.ppat.1006195>
19. Frieman, M., K. Ratia, R.E. Johnston, A.D. Mesecar, and R.S. Baric. 2009. Severe acute respiratory syndrome coronavirus papain-like protease ubiquitin-like domain and catalytic domain regulate antagonism of IRF3 and NF-KB signaling. *Journal of Virology*. 83: 6689–6705. <https://doi.org/10.1128/JVI.02220-08>
20. Krishnan, D.A., G. Sangeetha, S. Vajravijayan, N. Nandhagopal, and K. Gunasekaran. 2020. Structure-based drug designing towards the identification of potential anti-viral for covid-19 by targeting endoribonuclease NSP15. *Informatics in Medicine Unlocked*. 20: 100392. <https://doi.org/10.1016/j.imu.2020.100392>
21. Dominguez, C., R. Boelens, and A.M. Bonvin. 2003. Haddock: A protein–protein docking approach based on biochemical or biophysical information. *Journal of the American Chemical Society*. 125: 1731–1737.  
<https://doi.org/10.1021/ja026939x>
22. de Vries, S.J., M. van Dijk, and A.M. Bonvin. 2010. The haddock web server for data-driven biomolecular docking. *Nature Protocols*. 5: 883–897.  
<https://doi.org/10.1038/nprot.2010.32>
23. Tian, W., C. Chen, X. Lei, J. Zhao, and J. Liang. 2018. CASTp 3.0: Computed atlas of surface topography of proteins. *Nucleic Acids Research*. 46. <https://doi.org/10.1093/nar/gky473>
24. Bovijn, C., A.-S. Desmet, I. Uyttendaele, T. Van Acker, J. Tavernier, and F. Peelman. 2013. Identification of binding sites for myeloid differentiation primary response gene 88 (MYD88) and toll-like receptor 4 in MyD88 adapter-like (MAL). *Journal of Biological Chemistry*. 288: 12054–12066.  
<https://doi.org/10.1074/jbc.M112.415810>
25. Ohnishi, H., H. Tochio, Z. Kato, K.E. Orii, A. Li, T. Kimura, H. Hiroaki, N. Kondo, and M. Shirakawa. 2009. Structural basis for the multiple interactions of the MYD88 TIR domain in TLR4 signaling. *Proceedings of the National Academy of Sciences*. 106: 10260–10265. <https://doi.org/10.1073/pnas.0812956106>
26. Kim, Y., R. Jedrzejczak, N.I. Maltseva, M. Wilamowski, M. Endres, A. Godzik, K. Michalska, and A. Joachimiak. 2020. Crystal structure of NSP15 endoribonuclease nendou from SARS-CoV -2. *Protein Science*. 29: 1596–1605. <https://doi.org/10.1002/pro.3873>
27. Bhardwaj, K., P. Liu, J.L. Leibowitz, and C.C. Kao. 2012. The coronavirus endoribonuclease NSP15 interacts with retinoblastoma tumor suppressor protein. *Journal of Virology*. 86: 4294–4304. <https://doi.org/10.1128/JVI.07012-11>

28. Sinha, S.K., A. Shakya, S.K. Prasad, S. Singh, N.S. Gurav, R.S. Prasad, and S.S. Gurav. 2020. An in-silico evaluation of different Saikosaponins for their potency against SARS-COV-2 using NSP15 and fusion Spike glycoprotein as targets. *Journal of Biomolecular Structure and Dynamics*. : 1–12.  
<https://doi.org/10.1080/07391102.2020.1762741>
29. Holm, L., and L.M. Laakso. 2016. Dali Server update. *Nucleic Acids Research*. 44. <https://doi.org/10.1093/nar/gkw357>
30. Drozdetskiy, A., C. Cole, J. Procter, and G.J. Barton. 2015. JPRED4: A protein secondary structure prediction server. *Nucleic Acids Research*. 43.  
<https://doi.org/10.1093/nar/gkv332>
31. Yin, Q., S.-C. Lin, B. Lamothe, M. Lu, Y.-C. Lo, G. Hura, L. Zheng, R.L. Rich, A.D. Campos, D.G. Myszka, M.J. Lenardo, B.G. Darnay, and H. Wu. 2009. E2 interaction and dimerization in the crystal structure of TRAF6. *Nature Structural & Molecular Biology*. 16: 658–666. <https://doi.org/10.1038/nsmb.1605>
32. Lindahl, Abraham, Hess, and van der Spoel. 2021. Gromacs 2021.3 manual. Zenodo. <https://doi.org/10.5281/zenodo.5053220>